# Dynamic Spreading of Nanofluids on Solids Part II: Modeling

Kuan-Liang Liu,[†] Kirtiprakash Kondiparty, Alex D. Nikolov, and Darsh Wasan*

Department of Chemical and Biological Engineering, Illinois Institute of Technology, Chicago, Illinois 60616, United States

ABSTRACT: Recent studies on the spreading phenomena of liquid dispersions of nanoparticles (nanofluids) have revealed that the self-layering and two-dimensional structuring of nanoparticles in the three-phase contact region exert structural disjoining pressure, which drives the spreading of nanofluids by forming a continuous wedge film between the liquid (e.g., oil) and solid surface. Motivated by the practical applications of the phenomenon and experimental results reported in Part I of this two-part series, we thoroughly investigated the spreading dynamics of nanofluids against an oil drop on a solid surface. With the Laplace equation as a starting point, the spreading process is modeled by Navier–Stokes equations through the lubrication approach, which considers the structural disjoining pressure, gravity, and van der Waals force. The temporal interface profile and advancing inner contact line velocity of nanofluidic films are analyzed through varying the effective nanoparticle concentration, the outer contact angle, the effective nanoparticle size, and capillary pressure. It is found that a fast and spontaneous advance of the inner contact line movement can be obtained by increasing the nanoparticle concentration, decreasing the nanoparticle size, and/or decreasing the interfacial tension. Once the nanofluidic film is formed, the advancing inner contact line movement reaches a constant velocity, which is independent of the outer contact angle if the interfacial tension is held constant.
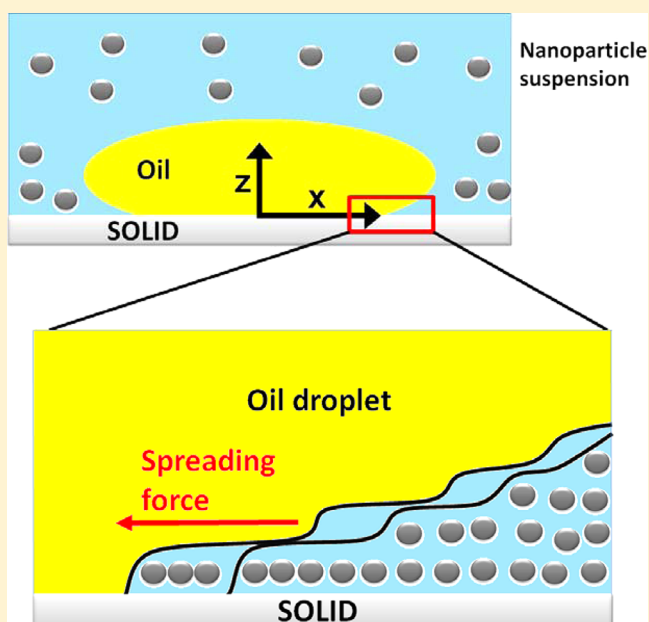
INTRODUCTION

The experimental data on the dynamic spreading behavior of silica nanofluids against an oil drop on a hydrophilic glass surface has been presented in Part I of this two-part series.[1] The experiments reveal that the nanofluid spreads spontaneously by forming an inner contact line that is not seen in pure liquids (without particles). In this paper, we analyze theoretically the movement of the advancing inner contact line and the effects of important technological parameters such as the nanoparticle concentration, particle size, contact angle, and capillary pressure on the contact line velocity.

The spreading of pure fluids against an oil droplet on a solid surface is generally characterized in terms of the spreading coefficient S:[2]

$$S = \sigma_{S/O} - \sigma_{S/L} - \sigma_{O/L} \tag{1}$$

where $\sigma_{S/O}$, $\sigma_{S/L}$, and $\sigma_{O/L}$ are, respectively, the interfacial tension existing between the solid–oil, solid–aqueous, and the oil–aqueous interfaces. When S is negative, the three-phase contact angle θ (defined as the outer contact angle) is established by force balance $\sigma_{S/O} = \sigma_{S/L} + \sigma_{O/L} \cos \theta$. The spontaneous spreading of a pure liquid occurs only when S is positive. In other words, the spreading of the aqueous phase is driven by the imbalance of the interfacial tensions.[3] Assuming

that the contact line movement friction force compensates for the imbalance of tensions, Kolev et al.[4] and Kralchevsky et al.[5] were able to dynamically model the spontaneous detachment of a hexadecane drop from a glass surface filled with an aqueous surfactant solution.

However, it has been shown that the classical theory of simple liquid spreading phenomena does not apply to nano- or complex fluids.[6–10] Theoretical calculations based on a series of Monte Carlo simulations and the statistical mechanics approach indicated that the particles near the vertex of a wedge-shaped wall tend to form a solid-like structure (Figure 1a); those far from the vertex have a fluid-like structure (more randomly packed).[11–13] The in-layer structure formation depends upon the position of the layer (i.e., confining film thickness) and bulk volume fraction of particles. Consequently, the osmotic component in the excess pressure (i.e., the film structural disjoining pressure) exerted by the self-layering and 2D structure of particles normal to the confining surfaces is higher near the vertex than that in the bulk region. With the structural disjoining pressure taken into account, the spreading coefficient
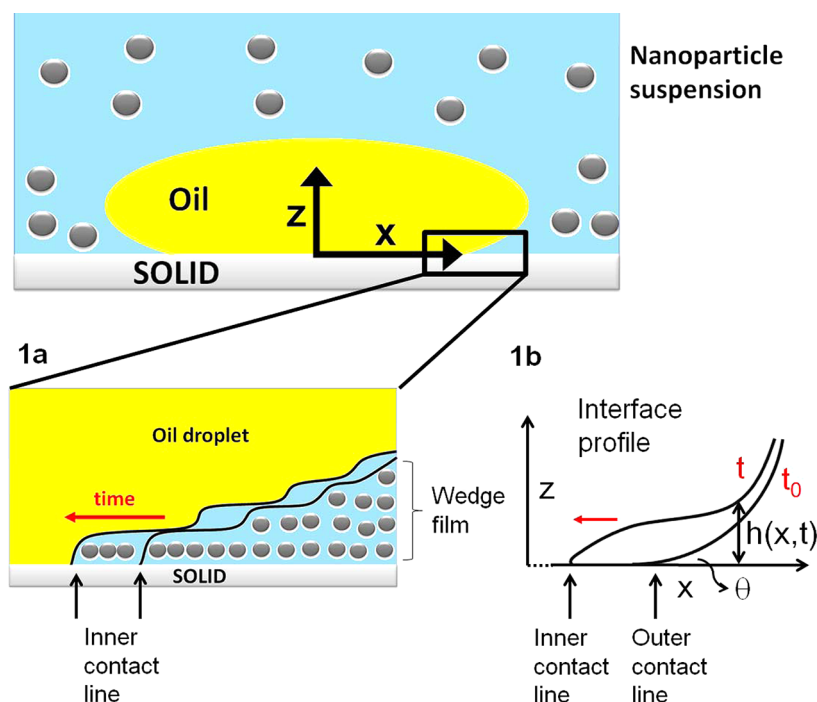
Figure 1. Schematic of (a) the spreading of nanoparticle suspension against an oil droplet and (b) the corresponding rectangular coordinates for mathematical treatment.

S of nanofluids is given by the Frumkin-Derjaguin equation as[14−19]

$$S = P_s(h_{eq})h_{eq} + \int_{h_{eq}}^{\infty} \Pi(h) \, dh = \sigma_{O/L}(\cos \theta_{eq} - 1) \tag{2}$$

where $P_s(h_{eq})$ represents the sum of the capillary pressure, P_c, and hydrostatic pressure, P_g, at the equilibrium film thickness, h_{eq}. Π is the disjoining pressure, including pressure due to the short-range van der Waals force, Π_{vdw}, the electrostatic force, Π_e, and the long-range structural force arising from the self-ordering of the nanoparticles in the wedge film region, Π_{st}. θ_{eq} is the equilibrium contact angle. The second term of the right side of eq 2, the integral of the disjoining pressure over the thickness of the wedge, represents the interaction energy between the surfaces (i.e., film tension or film energy).

The Frumkin-Derjaguin equation suggests that spontaneous spreading is achieved when $P(h_{eq})h_{eq} + \int_{h_{eq}}^{\infty}\Pi(h) \, dh \geq 0$, implying that structural disjoining pressure can play a role. On the basis of both experimental observations and calculations, Wasan and Nikolov[20] concluded that the driving force for the spreading of the nanofluids is the structural disjoining pressure gradient or film tension gradient directed toward the wedge from the bulk solution. As the film tension increases toward the vertex of the wedge (decreases the confining film thickness), it drives the nanofluid to spread at the wedge tip (inner contact line advances), therefore enhancing the spreading of nanofluids against another liquid phase on a solid substrate (Figure 1a).

Several theoretical studies have been conducted in the literature. Kralchevsky and Denkov[21] proposed a semiempirical relation for the structural disjoining pressure. Note that the structural disjoining pressure has an oscillatory decay with the increasing film thickness, and both the period of oscillation and decay factor are roughly the effective diameter (considering the hydration, double layer thickness, particle interaction, etc.) of the nanoparticle.[22,23] Chengara et al.[24] examined the spreading

of nanofluids on solid surfaces displacing an oil droplet using the modified Laplace equation. Kondiparty et al.[25] extended the static analysis, and concluded that the complete wetting and spontaneous spreading of the nanofluid against an oil droplet is achievable even with a considerable outer contact angle (∼30°). Nevertheless, spreading is a dynamic process.

The detailed dynamic analysis on the spontaneous spreading of nanofluids under the action of the disjoining pressure is very limited. To the best of our knowledge, the only relevant research study was conducted by Matar et al.[26] They studied the spreading dynamics of a nanofluid drop on a hydrophilic surface by adopting a lubrication approximation of mass and momentum conservation with consideration to the structural disjoining pressure. The spreading of nanofluids was assumed to be driven by the convective diffusion of nanoparticles in the wedge film.

Due to the versatile applications of the spreading phenomena in nanofluidics, advancing a fundamental understanding of the nanofluid spreading dynamics is necessary. This is done in the present paper by investigating the spreading of a nanofluid against an oil droplet on a hydrophilic surface. The simulation starts with the Laplace equation and is dynamically modeled by the Navier−Stokes equation with lubrication approach, which considers the structural disjoining pressure, gravity, and van der Waals force. For the first time, the spontaneous multistepwise profile and advancing inner contact line velocity of nanofluidic films are analyzed through varying the effective nanoparticle concentration, the outer contact angle, capillary pressure, and the effective nanoparticle size. The predicted behavior and values of the advancing inner contact line velocity are compared with experimental observations reported in Part I of this two-part series.[1] The results obtained are of significance to both fundamental knowledge and modern nanotechnology.

■ MODELING

As illustrated in Figure 1, we consider the spreading of nanofluids against an oil droplet on a hydrophilic solid surface. x and z are the rectangular coordinates adopted with their origin at the center of the solid−oil contact area. $h(x, t)$ is the vertical position of the oil−aqueous interface (i.e., the wedge film thickness near the three-phase contact region). The aqueous phase contains nanoparticles of effective diameter d_e (considering hydration, double layer thickness, particle interaction, etc.), with an effective nanoparticle volume fraction ϕ_e. For convenience, ϕ_e is assumed to be independent of position. We define the time domain t starting at the moment as the balance of $\sigma_{S/O}$, $\sigma_{S/L}$, and $\sigma_{O/L}$ is established with the outer contact angle θ in the absence of nanoparticles; afterward, the temporal deformation of the (inner) interface profile (i.e., $h(x, t)$) is modeled in the presence of the structural disjoining pressure.

Governing Equations. We adopted the lubrication theory[27] to study the fluid dynamics in this research because the vertical direction is significantly smaller than the horizontal direction. When the fluid inertia is neglected and the fluid pressure is independent of z, the Navier−Stokes equation leads to[26,27]

$$\frac{\partial}{\partial x}\left(P_o - P_w - \sigma\frac{\partial^2 h}{\partial x^2} - \Pi + P_g\right) = \frac{\partial}{\partial z}\left(\mu_f\frac{\partial u}{\partial z}\right) \tag{3}$$

In this equation, P_o and P_w represent the bulk pressure far from the wedge region of the oil and aqueous phases, respectively. $-\sigma(\partial^2 h/\partial x^2)$ is the capillary pressure with $\sigma = \sigma_{O/L}$ being the interfacial tension between the oil and the nanofluid. $P_g = \Delta\rho g(-h)$ is the hydrostatic pressure with $\Delta\rho$ and g being the density difference between the nanofluid and oil phase and the gravitation acceleration, respectively. μ_f is the film viscosity and u is the horizontal component of fluid velocity. We assumed that the film viscosity μ_f only depends on the effective nanoparticle concentration. The following boundary conditions are applied for u:

$$u = 0 \qquad \text{for } z = 0 \tag{4}$$

$$\mu_f\frac{\partial u}{\partial z} = -\frac{\partial W_{st}}{\partial x} \qquad \text{for } z = h \tag{5}$$

Equation 4 implies no-slip condition on the solid surface. Equation 5 is the tangential stress balance at the oil−nanofluid interface where W_{st} denotes the film energy arising from the self-structuring of nanoparticles due to the confinement. Integrating eq 3, subjected to the boundary conditions eqs 4 and 5, leads to the expression for $u(x, z)$:

$$u = -\frac{1}{\mu_f}\left[\frac{\partial}{\partial x}\left(\sigma\frac{\partial^2 h}{\partial x^2} + \Pi - P_g\right)\left(\frac{z^2}{2} - zh\right) + z\frac{\partial W_{st}}{\partial x}\right] \tag{6}$$

It is convenient to use the following scaling treatment: $x^* = x/L$, $z^* = z/H$, and $h^* = h/H$. The superscript $*$ is the dimensionless notation. $L(=100d_e)$ and $H(=d_e)$ are the characteristic film length and film thickness, respectively. H is equivalent to d_e due to the period of oscillation of the disjoining pressure, and hence the expected stepwise interface profile. The film aspect ratio $\varepsilon(=H/L)$ was chosen to be 0.01. Accordingly, $P(=\sigma\varepsilon^2/H)$ and $U(=\sigma\varepsilon^3/\mu_f)$ represent the characteristic pressure and velocity. In order to model the temporal

deformation of the interface profile, the following kinetic boundary condition is adopted:

$$\frac{\partial h^*}{\partial t^*} + \frac{\partial}{\partial x^*}\left(\int_0^{h^*} u^* \, dz^*\right) = 0 \tag{7}$$

where $t^* = t/\bar{t}$ and $u^* = u/U$ with $\bar{t} = (\mu_f d_e/\sigma\varepsilon^4)$ being the characteristic time. Substituting eq 6 into eq 7 leads to the following governing equation:

$$\frac{\partial h^*}{\partial t^*} = -\frac{\partial}{\partial x^*}\left[\frac{h^{*3}}{3}\frac{\partial}{\partial x^*}\left(\frac{\partial^2 h^*}{\partial x^{*2}} + \Pi^* - P_g^*\right) - \frac{h^{*2}}{2}\frac{\partial W_{st}^*}{\partial x^*}\right] \tag{8}$$

with $\Pi^* = \Pi/P$, $P_g^* = P_g/P$, and $W_{st}^* = W_{st}/(\sigma\varepsilon^2)$ being the scaled disjoining pressure, hydrostatic pressure and structural disjoining film energy, respectively. The scaled disjoining pressure $\Pi^*(=\Pi_{vdw}^* + \Pi_e^* + \Pi_{st}^*)$ including pressure due to the short-range van der Waals force, $\Pi_{vdw}^*(=\Pi_{vdw}/P)$, electrostatic force, $\Pi_e^*(=\Pi_e)/P$, and the long-range structural force, $\Pi_{st}^*(=\Pi_{st}/P)$. Let $\Pi_{vdw}^* = A^*/h^{*3}$ where $A^* = A/6\pi\varepsilon^2\sigma d_e^2$ is the van der Waals parameter with A being the Hamaker constant. The electrostatic force is negligible in this problem.[26]

We adopt the analytical expressions for the structural disjoining pressure and film energy given by Trokhymchuk et al.[22] based on solutions of the Ornstein−Zernike equation:

$$\Pi_{st}(h) = \Pi_1 \cos(\omega h + \varphi_2)\, e^{-\kappa h} + \Pi_2\, e^{-\delta(h-d_e)}$$
$$\text{for } h \geq d_e \tag{9a}$$

$$\Pi_{st}(h) = -\bar{P} \qquad \text{for } 0 < h < d_e \tag{9b}$$

$$W_{st}(h) = W_1 \cos(\omega h + \varphi_1)\, e^{-\kappa h} + W_2\, e^{-\delta(h-d_e)}$$
$$\text{for } h \geq d_e \tag{10a}$$

$$W_{st}(h) = \bar{P}(d_e - h) - 2\bar{\sigma} \qquad \text{for } 0 < h < d_e \tag{10b}$$

In these expressions, Π_1, Π_2, W_1, W_2, ω, φ_1, φ_2, κ, δ, $\bar{P}$, and $\bar{\sigma}$ are fitted as cubic polynomials in terms of the effective nanofluid volume fraction ϕ_e.[22] Figure 2 illustrates the structural disjoining pressure and film energy isotherms given by eqs 9a and 10a. As seen, the amplitude of the structural disjoining pressure and film energy increases with the increasing effective nanoparticle volume fraction and/or decreasing effective nanoparticle diameter. The oscillation period is roughly the effective nanoparticle diameter.

Numerical Procedure. As mentioned above, the present dynamic analysis starts at the moment when the outer contact line is balanced in the absence of nanoparticles, after the deformation of the interface, and hence inner contact line, are investigated through solving eqs 8−10b numerically. Let $h_0(x)$ be the vertical position of the oil−solid interface in the absence of the structural disjoining pressure (at $t = 0$). The interface profile as the outer contact line is established can be governed by Laplace equation:[24]

$$-\frac{\sigma(d^2 h_0/dx^2)}{\left[1 + (dh_0/dx)^2\right]^{3/2}} + P_g = P_w - P_o \tag{11}$$

With known parameters, including the apex radius of curvature of the oil drop, b, interfacial tension, σ, and outer contact angle, θ, eq 11, and hence $h_0(x)$, can be solved numerically from the apex (where $P_w - P_o = -\sigma/b$ and $dh_0/dx = 0$) to the solid
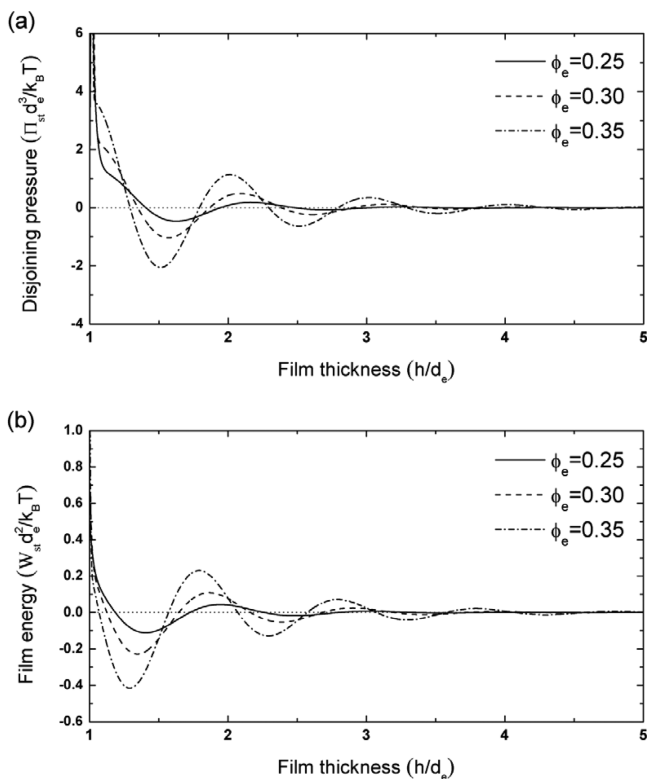
Figure 2. (a) Structural disjoining isotherms, and (b) film energy isotherms at various effective nanoparticle concentrations ϕ_e.[22] k_B and T are the Boltzmann constant and temperature, respectively.

surface (where $\tan^{-1}(dh_0/dx) = \theta$) by the explicit Runge-Kulta fifth method.[24] It should be pointed out that the capillary pressure term in eq 3 is different from that in eq 11, because $(dh/dx)^2 \ll 1$ in the wedge film and meniscus near the solid surface, thereby only the numerator $-\sigma(d^2h/dx^2)$ needs to be considered in eq 3. Then, eq 8 can be solved subject to the following initial condition:

$$h^*(x^*, 0) = h_0^*(x^*) \qquad \text{for } L_C^* \leq x^* \leq L_R^* \qquad (12a)$$

$$h^*(x^*, 0) = 0.01 \qquad \text{for } L_L^* \leq x^* \leq L_C^* \qquad (12b)$$

In these expressions, $h_0^* = h_0/H$. L_R^* and L_L^* are the right and left boundaries of the computational domain, respectively. Since the structural disjoining pressure and/or film tension are insignificant when the meniscus profile beyond four effective particle diameters from the solid surface (i.e., $h^* > 4$),[22,25] L_R^* is defined as the scaled horizontal position where $h_0^* = 5$. The length of the domain is set to be 50 (corresponding to 5000 times d_e); hence, $L_L^* = L_R^* - 50$. In eq 12b, a precursor layer with thickness 0.01 instead of zero is assumed, in order to obtain a finite value of the disjoining pressure. L_C^* is defined as the scaled horizontal position where $h_0^* = 0.01$. The boundary conditions for the governing equation can be expressed as

$$h^*(L_L^*, t^*) = 0.01, \quad \frac{\partial^2 h^*(L_L^*, t^*)}{\partial x^{*2}} = 0 \qquad (13a)$$

$$h^*(L_R^*, t^*) = h_0^*(L_R^*), \quad \frac{\partial^2 h^*(L_R^*, t^*)}{\partial x^{*2}} = \frac{\partial^2 h_0^*(L_R^*)}{\partial x^{*2}} \qquad (13b)$$

We solve the one-dimensional time-fractional governing equation, eq 8, subject to the initial condition, eqs 12a and 12b,

and boundary conditions, eqs 13a and 13b, numerically by applying the finite-difference method. Central difference discretization is adopted for spatial derivatives except for the points at the boundaries. The accuracy of the numerical analysis depends upon the grid density. In the computational domain of the present problem, if the number of grids exceeds ca. 1000, the results are roughly grid-independent with negligible error.

Note that, due to the compact packing of nanoparticles and/or the confinement effect in the wedge film, the film viscosity $\mu_f(\phi_e)$, expected to be much higher than that in the bulk solution, is unknown at this stage. The results shown are based on a scaled time domain $t^* = t/(\mu_f d_e/\sigma\varepsilon^4)$; however, in the last part of this paper, we estimate the film viscosity by comparing the results with the experimental data in order to obtain the real-time dynamic analysis and justify the present model.

■ RESULTS AND DISCUSSION

The spontaneous spreading process is examined through varying the effective nanoparticle concentration, the outer contact angle, the capillary pressure, and the effective nanoparticle size. For illustration, we set the Hamaker constant $A = 5 \times 10^{-21}$ J, the apex radius of curvature of oil drop $b = 500$ μm, and the density difference between nanofluid and oil phase $\Delta\rho = 0.212$ g/cm^3.

The temporal oil−nanofluid interface profile in the wedge region for a typical case is shown in Figure 3. The dotted line
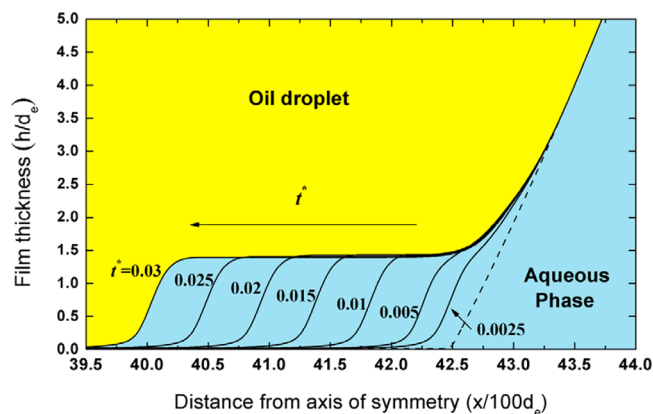

Figure 3. Temporal oil−nanofluid interface profile in the wedge region for the case $\phi_e = 0.25$, $\theta = 2°$, $\sigma = 2$ dyn/cm, and $d_e = 30$ nm. Dotted line: the interface profile at $t^* = 0$.

represents the case when $t^* = 0$ (i.e., when the meniscus is established in the absence of nanoparticles) serves as baseline given by eq 11. Note that this dotted line was justified by producing the same results as the static analysis of Chengara et al.[24] Solid lines present the (inner) interface profiles in the presence of nanoparticles as time increases. As the more compact structure is formed by the nanoparticles within a thinner confinement, the structural disjoining pressure and film energy increase toward the vertex of the wedge. This effect deforms the oil−nanofluid interface profile, forming a clear "step", and the inner contact line advances toward the center of the oil−solid contact area continuously.

The deformation and movement of the inner contact line can be understood by the structural disjoining pressure and film energy isotherms, as plotted in Figure 2. Note that the first term in eq 3 is zero (i.e., $P_o - P_w - \sigma\partial^2 h/\partial x^2 - \Pi + P_g = 0$ with $\Pi = 0$) in the absence of nanoparticles (as $t = 0$). When

nanoparticles self-organize as an ordered structure in the wedge region, they exert extra structural disjoining pressure on the oil−nanofluid interface. In other words, the interface deforms in order to achieve the new pressure balance by altering the capillary pressure. The structural disjoining pressure is insignificant at $h^*(h/d_e) \geq 3$ in this case, so the interface was almost fixed. The negative value of the structural disjoining pressure at $h^* \approx 1.5$ (as seen in Figure 2a) implies a depletion force; hence, the interface deforms (increase curvature) to increase the capillary force. However, the depletion force is too large to be balanced by the capillary pressure unless the profile retracted upward into the oil phase (where the spreading coefficient S is positive and θ_{eq} does not exist in eq 2), which is practically impossible; therefore, a continuously advancing step wedge-film forms. As indicated by Figure 3, when t^* is larger than 0.005, only one transition layer of particles parallel to the solid surface (wedge film) continuously advances, implying structural disjoining pressure at $h^* > 1.5$ had been balanced by the capillary pressure. The wedge-film thickness is roughly 1.4, close to the thickness of the minimum film energy state, as shown in Figure 2b. Since we focus on the structural disjoining pressure phenomena, it is advantageous to define the contact line position X_c (from the center of the oil−solid contact area) as the horizontal position where the thickness of the wedge equals one effective particle diameter

$$X_c^*(t^*) = x^*(h^* = 1, t^*) \tag{14}$$

where $X_c^* = X_c/L$ is the scaled contact line position. The scaled advancing inner contact line velocity $V_c^*(=V_c/U)$ can be expressed by

$$V_c^* = -\frac{dX_c^*(t^*)}{dt^*} \tag{15}$$

We found that the advancing inner contact line velocity becomes constant after a short period ($t^* \approx 0.01$, in this case), and so for the first time, it is consistent with the experimental observation.[1] In the following subsections, we discussed the effects of the parameters on the temporal interface profile and the advancing inner contact line velocity; these parameters include the effective nanoparticle concentration, the outer contact angle, the oil−nanofluid tension, and the effective nanoparticle size.

Effect of the Nanoparticle Volume Fraction ϕ_e. Figure 4 illustrates the oil−nanofluid interface profile at $t^* = 0.02$ with varying effective nanoparticle concentrations. When the aqueous phase contains more nanoparticles, it has been shown that the structuring effect due to the confinement in the wedge region is stronger.[11] Figure 2 also suggests that the amplitudes of both the structural disjoining pressure and the film energy increase with the increasing effective nanoparticle concentration. Thus, the inner contact line movement is faster with a higher effective nanoparticle concentration during the same period of time. At high concentrations (i.e., $\phi_e \geq 0.25$), the interface is concave at $h^* \approx 1-1.4$, convex at $h^* \approx 1.4-1.6$ and again concave at $h^* \approx 2.0$ when viewed from the aqueous phase. Higher nanoparticle concentrations yield a more profound phenomenon. This results from the spontaneous deformation of the interface (tuning capillary pressure) corresponding to the positive−negative−positive value of the structure disjoining pressure, as shown in Figure 2a. It is important to note that the higher effective nanoparticle concentrations result in a more compact structure self-
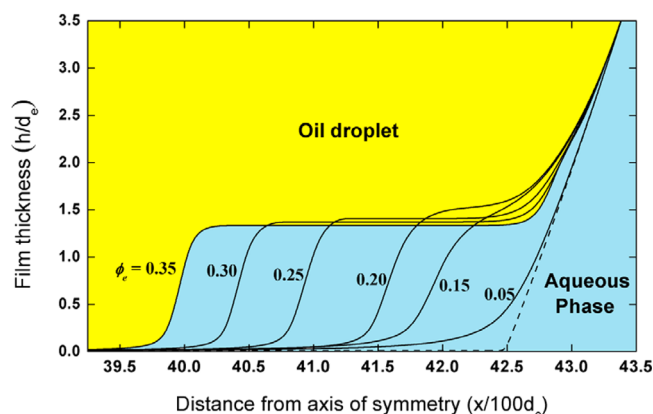

Figure 4. Oil−nanofluid interface profiles in the wedge region at $t^* = 0.02$ with various effective nanoparticle concentrations, ϕ_e, for the case $\theta = 2°$, $\sigma = 2$ dyn/cm, and $d_e = 30$ nm. Dotted line: the interface profile at $t^* = 0$.

organized by the nanoparticles, so the films have the minimum film energy with the thinner thickness, as shown in Figure 2b. This is also revealed in Figure 4, where the wedge-film thickness decreases with higher effective nanoparticle concentrations. For the case $\phi_e = 0.05$, the structural disjoining pressure is too small to affect the interface profile, as the contact line position $X_c^*(t^*)$ is barely changed. Note that the deformation at $h^* \approx 0-1.0$ for the case $\phi_e = 0.05$ is due to the presence of the precursor layer and van der Waals contribution.

Figure 5 plots the scaled contact line position as a function of the scaled time for the cases in Figure 4. $X_c^*(t^* = 0)$ represents
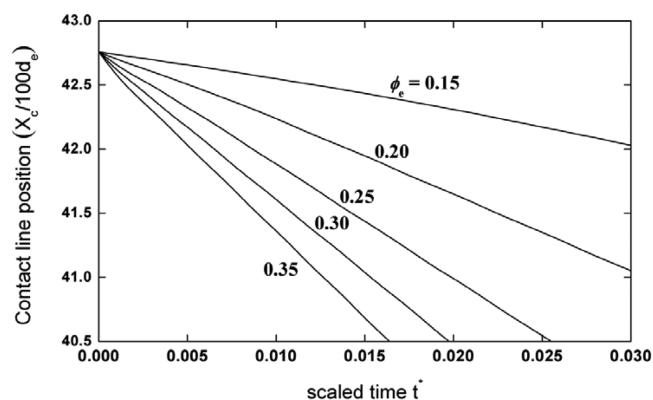

Figure 5. Scaled contact line position, $X_c^* = X_c/100d_e$, as a function of the scaled time t^* with various effective nanoparticle concentrations, ϕ_e, for the case in Figure 4.

the outer contact position (from the center of oil−solid contact area). As seen, the contact line position decreases as the inner contact line advances with time (it gets closer to the center of oil−solid contact area). The linear dependences imply that the inner contact line velocity is constant in every case except in the beginning, and the slopes are the scaled inner contact line velocities. The scaled inner contact line velocities V_c^* for $\phi_e = 0.15, 0.20, 0.25, 0.30, 0.35$ are, respectively, 26, 59, 89, 113, 135.

Effect of the Outer Contact Angle θ. Kondiparty et al.[25] suggested that the nanofluid completely spreads as a horizontal film between the oil droplet and solid surface, even at a finite outer contact angle in the presence of the structural disjoining pressure. They also pointed out that there exists a critical outer contact angle θ_c (which depends upon ϕ_e, σ, and d_e),[25] beyond

which the structural disjoining pressure is balanced by capillary pressure without establishing a horizontal fluidic film, and the nanofluid cannot spontaneously spread. The scaled contact line position X_c^* as a function of the scaled time with various outer contact angles θ (all θ are below θ_c) is plotted in Figure 6. As
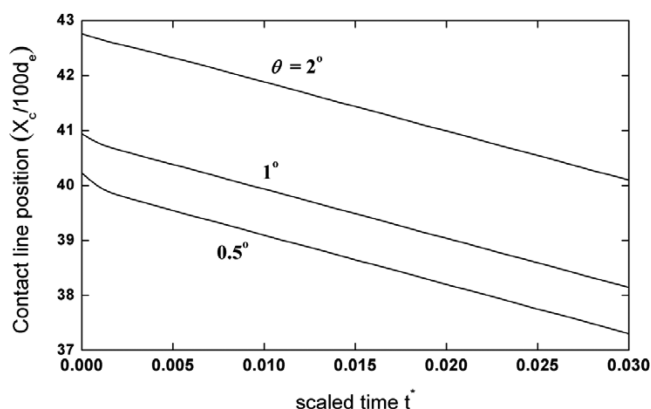

Figure 6. Scaled contact line position, $X_c^* = X_c/100d_e$, as a function of the scaled time t^* with various outer contact angles, θ, for the case $\phi_e = 0.25$, $\sigma = 2$ dyn/cm, and $d_e = 30$ nm.

seen, with a fixed apex radius of curvature, b, and interfacial tension, σ, different outer contact line positions X_c^* at $t^* = 0$ is established by the Laplace equation (eq 11) with various θ. The different meniscus profiles result in different inner contact line velocities at the beginning stage. This suggests that the more hydrophilic surfaces aid in spreading the nanofluid on the solid surface, as also found by Kondiparty et al.[25]

Figure 6 indicates that the inner contact line velocity reaches a constant value after a certain period of time; moreover, the velocities for these three cases are identical ($V_c^* = 89$). This is because, once a horizontal film is established (when $\theta < \theta_c$), the advancing inner contact line is not affected by the outer meniscus profile. For instance, referring to the case $\theta = 2°$ (Figure 3), when $t^* > 0.01$, once the wedge film parallel to the solid surface is established, only then does the inner contact region move, which should physically only be governed by the effective nanoparticle concentration ϕ_e, oil−nanofluid interfacial tension σ, and effective nanoparticle size, d_e. Note that the outer contact angle physically depends upon the interfacial tensions among the three phases in real systems, and the results shown in Figure 6 are based on the same oil−nanofluid interfacial tension σ.

Effect of the Oil−Nanofluid Interfacial Tension σ. The spreading of nanofluids due to the structural disjoining pressure

(and film tension) gradient is resisted by the capillary pressure. Hence, for the same nanoparticle concentration, the slower inner contact line velocity with a higher capillary pressure is expected. This is validated by comparing the results shown in Figures 3 and 7. Figure 7 illustrates the temporal oil−nanofluid interface profile in the wedge region at $\sigma = 10$ and 20 dyn/cm, while Figure 3 illustrates the case $\sigma = 2$ dyn/cm (the other parameters are fixed). Apparently, higher levels of the interfacial tension (higher capillary pressure) result in slower advancing inner contact line movement. The scaled inner contact line velocities V_c^* for $\sigma = 2, 10, 20$ dyn/cm are, respectively, 89, 17, 7. However, it should be noted that the characteristic velocity $U(=\sigma\varepsilon^3/\mu_f)$ includes the interfacial tension σ. Therefore, it is better to compare the inner contact line velocity with units, where the products of $V_c\mu_f$ for $\sigma = 2, 10, 20$ dyn/cm are, respectively, 0.18, 0.17, 0.14 mm/s × cp. This also suggests that a higher inner contact velocity can be obtained with a smaller capillary pressure (which is consistent with the experimental observations; see Figures 6−8 in Part I[1]). In this case, the slight difference of velocities between $\sigma = 2$ and 10 dyn/cm implies that the capillary pressure is much smaller than structural disjoining pressure when $\sigma < 10$, and hence, the interfacial tension merely affects the inner contact line velocity.

Effect of the Nanoparticle Diameter d_e. The variations of the scaled inner contact line velocity V_c^* as a function of the effective nanoparticle concentration ϕ_e with varying effective nanoparticle diameters d_e is presented in Figure 8. The effective

Figure 8. Variations of the scaled inner contact line velocity V_c^* as a function of the effective nanoparticle concentration ϕ_e with various effective nanoparticle diameters d_e at $\theta = 2°$ and $\sigma = 2$ dyn/cm.

nanoparticle diameter varies from 15 to 40 nm. Higher concentrations result in faster inner contact line movement. It also suggests that smaller nanoparticles yield greater inner contact line velocities. For the same nanoparticle volume
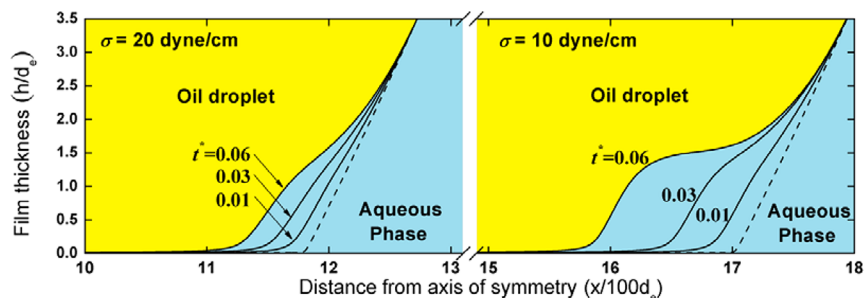
Figure 7. Temporal oil−nanofluid interface profile in the wedge region at $\sigma = 10$ and 20 dyn/cm for the case $\phi_e = 0.25$, $\theta = 2°$, and $d_e = 30$ nm. Dotted line: the interface profile at $t^* = 0$.

concentration, the concentration of nanoparticles is higher with the smaller particle sizes, so more particles are expected to be pumped into the wedge region by the entropic force. According to the theoretical work of Trokhymchuk et al.,[22] the structural disjoining pressure and film energy isotherms are in reverse proportion to the cube of the effective particle diameter for a fixed effective nanoparticle volume concentration.

The inner contact line velocity merely depends upon the contact angle and interfacial tension when the structural disjoining pressure is much higher than the capillary pressure, as discussed above. Hence, the results in Figure 8 can be adopted to predict the contact line velocity with a given effective nanoparticle concentration and effective particle diameter. By fitting the data points in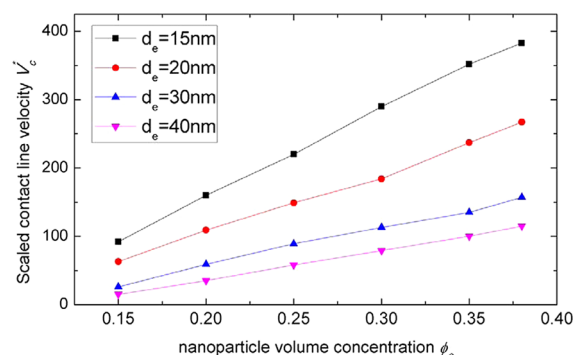 Figure 8, an expression of the scaled inner contact line velocity as a function of the effective nanoparticle concentration and effective particle size can be obtained as

$$V_c^* = 24605 \frac{\phi_e}{(d_e/nm)^{1.105}} - \left[\frac{1268}{(d_e/nm)^2} - \frac{50}{(d_e/nm)} + 7.5607 \right]^2 \tag{16}$$

The coefficient of regression, R^2, of the fitted expression is roughly 0.99. Multiplying eq 16 by $\sigma\varepsilon^3$ leads to the expression of the product of the inner contact line velocity and film viscosity:

$$V_c\mu_f(mm/s \cdot cp) = 49.2 \frac{\phi_e}{(d_e/nm)^{1.105}} - \left[\frac{56.7}{(d_e/nm)^2} - \frac{2.24}{(d_e/nm)} + 0.338 \right]^2 \tag{17}$$

The film viscosity μ is unknown, and will be estimated in the last section by comparing the present results with the experimental data.

Using a larger nanoparticle concentration and/or smaller particle size not only obtains a faster advancing inner contact line velocity, but also leads to an important feature of spreading, the multistepwise phenomena, as shown in Figure 9. In an experiment with tiny drops spreading on a silicon wafer, Heslot et al.[28] found that the droplet advanced as a series of distinct
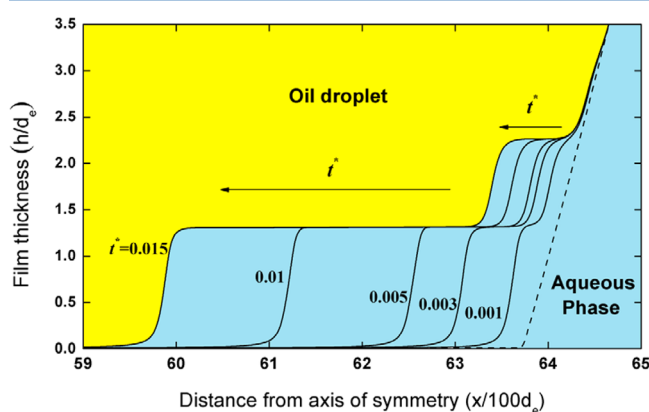

Figure 9. Temporal oil−nanofluid interface profile in the wedge region for the case $\phi_e = 0.38$, $\theta = 2°$, $\sigma = 2$ dyn/cm, and $d_e = 20$ nm. Dotted line: the interface profile at $t^* = 0$.

molecular layers through ellipsometry. Nikolov and Wasan[29] illustrated multilayer stratification in thinning foam films formed from micellar solutions. Also, Nikolov et al.[30] used a silica nanoparticle suspension and reflected light interferometry, and observed the multilayer phenomena during the film thinning on a glass surface.

Figure 9 shows the temporal oil−nanofluid interface profile in the wedge region for the case with two transition layers of particles. Compare this to the case in Figure 3; we increased the effective nanoparticle concentration from 0.25 to 0.38, and decreased the effective particle diameter from 30 to 20 nm. During this change, the corresponding structural disjoining pressure (at the maximum depletion pressure) was increased from 1.5×10^3 to 3.3×10^4 dyn/cm^2 (i.e., 22 times higher). As suggested in Figure 2a, when the nanoparticle concentration is high ($\phi_e = 0.35$), the depletion pressure at $h^* \approx 2.5$ is also profound. When such a depletion pressure cannot be balanced by the capillary pressure, it forms a wedge film containing two transition layers. As indicated in Figure 9, the wedge film containing two transition layers with a thickness $h^* \approx 1.3$ (with one horizontal layer of particles) and $h^* \approx 2.3$ (with two horizontal layers of particles) advances continuously. A similar film geometry was also found in the experimental results, where Nikolov et al.[30] recently reported that, for a nanoparticle with an effective diameter 43 nm, the thicknesses of first and second layers are, respectively, 66 nm ($h^* \approx 1.5$) and 107 nm ($h^* \approx 2.5$). Note that the advancing velocity for the first layer is higher than that of the second layer, simply because the structural disjoining pressure is much stronger with the thinner confinement.

■ COMPARISON WITH EXPERIMENTAL DATA

Experimental results for the spreading of nanofluids composed of silica particles of a nominal (or geometric) diameter $d = 19$ nm with nominal particle volume concentrations of 5% ($\phi = 0.05$), 10% ($\phi = 0.1$), and 20% ($\phi = 0.2$) against 0.13 μL canola oil droplets are shown in Figures 6−8 in Part I[1] and summarized in Table 1. To compare the present model with this experimental data, we estimate the effective particle diameter d_e and effective nanoparticle concentration ϕ_e. Because the excluded volume for particles includes the double layer thickness, both the effective nanoparticle diameter and the volume concentration are expected to be higher than the nominal values. The effective particle diameter can be found as the thickness difference between the first and second transition layer of the wedge in the same experiment; for example, the difference is 43 nm for the case $\phi = 0.1$.[30,31] Nikolov and Wasan[31] also found that the number of transition layers for $\phi = 0.05, 0.1, 0.2$ are, respectively, 1, 3, 4; the corresponding effective volume concentration can be estimated as 0.4, 0.45, 0.66.[31]

It should be pointed out that, in the present model, the expression of the structural disjoining pressure and film energy proposed by Trokhymchuk et al.[22] was based on the assumptions that the particles are monodispersed. Polydispersity significantly affects the structural disjoining pressure. Chu et al.[32] reported that the structural force with a 25% polydispersity was roughly 45% of the monodispersed one. Considering the polydispersity and solvent effect in our real experimental system, we corrected the effective nanoparticle concentration. This was done with the help of results from the recent experiments performed by Nikolov et al.,[30] who combined Frumkin-Derjaguin equation with the experimental

Table 1. Properties of the Nanofluid and Inner Contact Line Velocity in the Experimental Data of Part I of This Two-Part Series[1]

		nanoparticle volume		
concentration ϕ	effective volume concentration ϕ_e	corrected effective concentration ϕ_e	effective nanoparticle diameter d_e (nm)	advancing inner contact line velocity V_c (mm/s)
0.05	0.40	0.27	50 nm	2.6×10^{-4}
0.1	0.45	0.30	43 nm	3.6×10^{-4}
0.2	0.66	0.44	30 nm	4.5×10^{-4}

Table 2. List of Parameters, Corresponded Viscosity, and Inner Contact Line Velocity

effective diameter d_e (nm)	effective volume ϕ_e	contact angle θ (deg)	interfacial tension σ (dyn/cm)	scaled contact line velocity $V_c{}^*$	(eq 20) film viscosity μ_f (cp)	contact line velocity V_c (mm/s)	(eq 21) contact line velocity V_c (mm/s)
15	0.15	2	2	92			
15	0.20	2	2	160	304	1.05×10^{-3}	9.78×10^{-4}
15	0.25	2	2	220	324	1.36×10^{-3}	1.30×10^{-3}
15	0.30	2	2	290	364	1.59×10^{-3}	1.50×10^{-3}
15	0.35	2	2	352	440	1.60×10^{-3}	1.51×10^{-3}
15	0.38	2	2	383	517	1.48×10^{-3}	1.43×10^{-3}
20	0.15	2	2	63			
20	0.20	2	2	109	304	7.17×10^{-4}	7.31×10^{-4}
20	0.25	2	2	149	324	9.18×10^{-4}	9.61×10^{-4}
20	0.30	2	2	184	364	1.01×10^{-3}	1.10×10^{-3}
20	0.35	2	2	237	440	1.08×10^{-3}	1.12×10^{-3}
20	0.38	2	2	267	517	1.04×10^{-3}	1.05×10^{-3}
30	0.15	2	2	26			
30	0.20	2	2	59	304	3.88×10^{-4}	4.01×10^{-4}
30	0.25	2	2	89	324	5.50×10^{-4}	5.52×10^{-4}
30	0.25	1	2	89	324	5.50×10^{-4}	5.52×10^{-4}
30	0.25	0.5	2	89	324	5.50×10^{-4}	5.52×10^{-4}
30	0.25	2	10	17	324	5.24×10^{-4}	
30	0.25	2	20	7	324	4.31×10^{-4}	
30	0.30	2	2	113	364	6.20×10^{-4}	6.48×10^{-4}
30	0.35	2	2	135	440	6.12×10^{-4}	6.66×10^{-4}
30	0.38	2	2	157	517	6.06×10^{-4}	6.34×10^{-4}
40	0.15	2	2	15			
40	0.20	2	2	35	304	2.30×10^{-4}	2.14×10^{-4}
40	0.25	2	2	58	324	3.57×10^{-4}	3.29×10^{-4}
40	0.30	2	2	79	364	4.33×10^{-4}	4.07×10^{-4}
40	0.35	2	2	100	440	4.54×10^{-4}	4.32×10^{-4}
40	0.38	2	2	115	517	4.44×10^{-4}	4.16×10^{-4}

data of the film meniscus running angle to calculate the structural disjoining film energy isotherm. The estimated film energy ($W_{st}d_e^2/k_BT$) of the first layer in the case $\phi = 0.1$ was -0.25, corresponding to the energy state given by the expression of the structural disjoining film energy with $\phi_e = 0.30$ (eq 10a, the minimum energy at $h^* \approx 1.4$). Therefore, $\phi_e = 0.30$ was the effective nanoparticle concentration used in the present model. The same corrected ratio ($0.30/0.45 = 0.66$) was applied to the other cases ($\phi = 0.05$ and 0.2) used in the experiments reported in Part I.[1]

Estimating Film Viscosity. The film viscosity μ_f is a function of the effective nanoparticle concentration. As suggested by the Frenkel equation,[33] the film viscosity is an exponential function of the energy barrier between two adjacent particles. The energy barrier is found to increase with the increasing value of the nanoparticle concentration.[34,35] Thus, we assume the following generalized exponential equation for the variation of the film viscosity with the effective nanoparticle concentration

$$\mu_f(\phi_e) = C \exp\left(\frac{-W_{st,1}(\phi_e)d_e^2}{k_BT}\right) \tag{18}$$

where C is a pre-exponential constant, independent of the nanoparticle concentration. The energy barrier between two adjacent particles can be characterized by the film energy. As discussed above, the film thickness (of the first transition layer) is close to the thickness with a minimum film energy (at $h^* \approx 1.2-1.5$, and depends upon ϕ_e), as shown in Figure 2b or given by eq 10a. Hence, the film energy of the first transition layer, denoted by $W_{st,1}(\phi_e)$, can be estimated as the minimum value of the film energy isotherm. We found the variation of $W_{st,1}(\phi_e)$, given by eq 10a as a function of the effective nanoparticle concentration can be fitted with a power function as

$$\frac{-W_{st,1}(\phi_e)d_e^2}{k_BT} = 25.4 \cdot \phi_e^{3.91} \tag{19}$$

The pre-exponential constant C in eq 18 is then determined by one of the three experimental data points. Fitting the experimental results of the case $\phi = 0.1$ ($\phi_e = 0.30$, $d_e = 43$ nm, $V_c = 3.6 \times 10^{-4}$ mm/s) by eqs 17−19, the constant C and film viscosity μ_f ($\phi_e = 0.30$) are 290 and 364 cP, respectively. Note that nanoparticles form a well-ordered 2D cubic or hexagonal structure;[11] therefore, a high viscosity is expected. The same order of viscosity, ∼160 cP, was estimated by Basheva et al.[36] through a vertical film stepwise drainage experiment. Substituting eq 19 and C into eq 18 leads to the expression of the film viscosity

$$\mu_f(\phi) = 290 \exp(25.4\phi_e^{3.91}) \tag{20}$$

The expression of inner contact line velocity can be obtained by combining eqs 17 and 20 as

$$\frac{V_c}{(\text{mm/s})} = \left\{ \frac{0.169\phi_e}{(d_e/\text{nm})^{1.105}} \right.$$
$$\left. - \left[\frac{3.33}{(d_e/\text{nm})^2} - \frac{0.132}{(d_e/\text{nm})} + 0.0199 \right]^2 \right\}$$
$$\exp(-25.4\phi_e^{3.91}) \tag{21}$$

Note that the film viscosity given by eq 20 apparently overestimates the value when the nanoparticle concentration is small (μ should approach 1 cP as $\phi_e \to 0$). The structural disjoining pressure and film energy expression, eqs 9a, 9b and 10a,10b, are unrealistic when ϕ_e is beyond 0.4.[22] Thus, eq 21 can only be applied in the range $0.20 < \phi_e < 0.40$ and when the structural disjoining pressure is much higher than the capillary pressure (i.e., when the contact line velocity is not significantly affected by the interfacial tension).

The prediction of eq 21, and of the present theoretical work, is validated by predicting the other experimental data using eq 21. The predicted contact line velocity for the case $\phi = 0.05$ ($\phi_e = 0.27$, $d_e = 50$ nm) given by eq 21 is 2.23×10^{-4} mm/s, close to the experimental data, 2.6×10^{-4} mm/s (Table 1). This illustrates the validity of the present model.

It should be stated that, for the other case of $\phi = 0.2$ ($\phi_e = 0.43$, $d_e = 30$ nm), the effective nanoparticle concentration is beyond the applicability range of eq 21 as mentioned above, so it is not possible to obtain a reliable prediction.

We summarize the results of the parametric study in Table 2, including the parameters, scaled contact line velocity from our model, film viscosity given by eq 20, and the corresponding contact line velocity. The velocity in the last column is directly calculated by eq 21. Note that Matar et al.[26] reported that increasing nanoparticle concentration also decreases the spreading velocity due to the larger viscosity. This is also found in the present study. As indicated, when $\phi_e \geq 0.35$, further increasing nanoparticle concentration will increase the film viscosity significantly, therefore decreasing the contact line velocity. This extreme concentration needs further experimental verification.

◼ CONCLUSIONS

We analyzed theoretically the spreading dynamics of nanoparticle suspensions (nanofluids) against oil drops on a solid surface. For the first time, we present the model results which present both the temporal interface profile and advancing inner contact line velocity of nanofluidic film. Consistent with the

Table 3. List of Nomenclature

A	Hamaker constant (J)
A^*	$=A/6\pi\varepsilon^2\sigma d_e^2$ (-)
b	apex radius of curvature of the oil drop (μm)
d_e	effective nanoparticle diameter (m)
k_B	Boltzmann constant (J/K)
g	gravitational acceleration (m/s^2)
H, L	characteristic film thickness and length, $=d_e$, $=100d_e$ (nm)
$h(x, t)$	vertical position of the oil-aqueous interface (nm)
$h_0(x)$	vertical position of the oil−aqueous interface at $t = 0$ (nm)
h^*, h_0^*	$=h/H$, $=h_0/H$ (-)
L_c^*	scaled horizontal position when $h_0^* = 0.01$ (-)
L_R^*, L_L^*	right and left boundaries of the computational domain (-)
P	characteristic pressure $=\sigma\varepsilon^2/H$ (Pa)
P_c	capillary pressure (Pa)
P_g	hydrostatic pressure $=\Delta\rho g(-h)$ (Pa)
P_g^*	$=P_g/P$ (-)
P_o, P_w	bulk pressure far from the wedge of oil and aqueous phases (Pa)
P_s	$=P_C + P_g$ (Pa)
S	spreading coefficient $=\sigma_{S/O} - \sigma_{S/L} - \sigma_{O/L}$ (dyn/cm)
T	temperature (k)
t	time domain (s)
$\bar{t}$	characteristic time $=\mu_f d_e/\sigma\varepsilon^4$ (s)
t^*	$=t/\bar{t}$ (-)
U	characteristic velocity $=\sigma\varepsilon^3/\mu_f$ (mm/s)
u	horizontal component of fluid velocity (mm/s)
u^*	$=u/U$ (-)
V_c	inner contact line velocity (mm/s)
V_c^*	scaled inner contact line velocity $= V_c/U$ (-)
W_{st}	film energy arising from the structural force (J/m^2)
$W_{st,1}$	film energy of the first transition layer (J/m^2)
W_{st}^*	$=W_{st}/(\sigma\varepsilon^2)$ (-)
x, z	rectangular coordinates (m)
x^*, z^*	$= x/L$, $= z/H$ (-)
$X_c(t)$	contact line position (m)
$X_c^*(t^*)$	$=X_c/L$ (-)
ε	film aspect ratio $=H/L$ (-)
ϕ, ϕ_e	geometric and effective nanoparticle volume fraction (-)
μ_f	wedge film viscosity (cp)
Π	disjoining pressure $=\Pi_{vdw} + \Pi_e + \Pi_{st}$ (Pa)
$\Pi_e, \Pi_{st}, \Pi_{vdw}$	disjoining pressure due to the van der Waals force, electrostatic force, the structural force (Pa)
$\Pi^*, \Pi_e^*, \Pi_{st}^*, \Pi_{vdw}^*$	$=\Pi/P$, $=\Pi_e/P$, $=\Pi_{st}/P$, $=\Pi_{vdw}/P$ (-)
θ	outer contact angle (degree)
θ_c	critical contact angle (degree)
θ_{eq}	equilibrium outer contact angle (degree)
$\Delta\rho$	density difference between the aqueous and oil phases (g/cm^3)
$\sigma_{S/O}, \sigma_{S/L}, \sigma_{O/L}$	interfacial tension between the solid−oil, solid−aqueous, oil−aqueous interfaces (dyn/cm)
$\Pi_1, \Pi_2, W_1, W_2, \omega, \varphi_1, \varphi_2, \kappa, \delta, \bar{P}, \bar{\sigma}$	fitted functions as cubic polynomials in terms of ϕ_e, ref 22 (-)

experimental observations,[1] constant velocities of inner contact line movement are obtained. The model also illustrates that the

multistepwise wedge film is formed because of the structural disjoining pressure effect. We find that the higher advancing inner contact line velocity can be achieved by increasing the effective nanoparticle concentration, decreasing the effective nanoparticle size, and/or decreasing the interfacial tension. The dependence of the interfacial tension on the inner contact line velocity is not significant when the structural effect is dominant. Once a continuously advancing wedge film is formed, the inner contact line velocity is independent of the outer contact angle as long as the interfacial tension is fixed.

The present paper also provides a semiempirical expression for the inner contact line velocity as a function of the effective nanoparticle size and volume concentration (eq 21). The model prediction for the inner contact line velocities favorably agree with the experimental observations in Part I of this two-part series.[1] Future experimental studies are warranted to further verify the model predictions. There is also a need to independently measure the viscosity of the nanoparticle structured thin film.

■ AUTHOR INFORMATION

Corresponding Author
*E-mail: wasan@iit.edu.

Present Address
†E-mail: f96524027@ntu.edu.tw.

Notes
The authors declare no competing financial interest.

■ ACKNOWLEDGMENTS

■ REFERENCES

(1) Kondiparty, K.; Nikolov, A. D.; Wasan, D. Dynamic Spreading of Nanofluids on Solids. Part I: Experimental. *Langmuir* **2012**, *28*, 14618−14623.

(2) de Gennes, P. G. Wetting: Statics and Dynamics. *Rev. Mod. Phys.* **1985**, *57*, 827−863.

(3) Semal, S.; Voué, M.; De Coninck, J. Dynamics of Spontaneous Spreading on Energetically Adjustable Surfaces in a Partial Wetting Regime. *Langmuir* **1999**, *15*, 7848−7854.

(4) Kolve, V. L.; Kochijashky, I. I.; Danov, K. D.; Kralchevsky, P. A.; Broze, G.; Mehreteab, A. Spontaneous Detachment of Oil Drops from Solid Subtrates: Governing Factors. *J. Colloid Interface Sci.* **2004**, *257*, 357−363.

(5) Kralchevsky, P. A.; Danov, K. D.; Kolev, V. L.; Gurkov, T. D.; Temelska, M. I.; Brenn, G. Detachment of Oil Drops from Solid Surfaces in Surfactant Solutions: Molecular Mechanisms at a Moving Contact Line. *Ind. Eng. Chem. Res.* **2005**, *44*, 1309−1321.

(6) Churaev, N. V. On the Forces of Hydrophobic Attraction in Wetting Films of Aqueous-Solutions. *Colloids Surf., A* **1993**, *79*, 25−31.

(7) Ruckenstein, E. Effect of Short-Range Interactions on Spreading. *J. Colloid Interface Sci.* **1996**, *179*, 136−142.

(8) Churaev, N. V.; Esipova, N. E.; Hill, R. M.; Sobolev, V. D.; Starov, V. M.; Zorin, Z. M. The Superspreading Effect of Trisiloxane Surfactant Solutions. *Langmuir* **2001**, *17*, 1338−1348.

(9) De Coninck, J.; de Ruijter, M. J.; Voué, M. Dynamics in Wetting. *Curr. Opin. Colloid Interface Sci.* **2001**, *6*, 49−53.

(10) Chaudhury, M. K. Complex Fluids - Spread the Word about Nanofluids. *Nature* **2003**, *423*, 131−132.

(11) Chu, X. L.; Nikolov, A. D.; Wasan, D. T. Monte Carlo Simulation of Inlayer Structure Formation in Thin Liquid Films. *Langmuir* **1994**, *10*, 4403−4408.

(12) Boda, D.; Chan, K. Y.; Henderson, D.; Wasan, D. T.; Nikolov, A. D. Structure and Pressure of a Hard Sphere Fluid in a Wedge-Shaped Cell or Meniscus. *Langmuir* **1999**, *15*, 4311−4313.

(13) Tata, B. V. R.; Boda, D.; Henderson, D.; Nikolov, A.; Wasan, D. T. Structure of Charged Colloids under a Wedge Confinement. *Phys. Rev. E* **2000**, *62*, 3875−3881.

(14) Frumkin, A. N. Wetting and Adherence of Bubbles. *Zh. Fiz. Khim.* **1938**, *12*, 337−345.

(15) Derjaguin, B. V. Theory of Capillary Condensation and Related Capillary Effects. Calculation of Spreading Action of Polymolecular Liquid Films. *Zh. Fiz. Khim.* **1940**, *14*, 137−147.

(16) Starov, V. M. Equilibrium and Hysteresis Contact Angles. *Adv. Colloid Interface Sci.* **1992**, *39*, 147−173.

(17) Churaev, N. V. Surface Forces in Wetting Films. *Adv. Colloid Interface Sci.* **2003**, *103*, 197−218.

(18) Churaev, N. V. Deryaguin's Disjoining Pressure in the Colloid Science and Surface Phenomena. *Adv. Colloid Interface Sci.* **2003**, *104*, xv−xx.

(19) Starov, V. M.; Velarde, M. G. Surface Forces and Wetting Phenomena. *J. Phys.: Condens. Matter* **2009**, *21* (464121), 1−11.

(20) Wasan, D. T.; Nikolov, A. D. Spreading of Nanofluids on Solids. *Nature* **2003**, *423*, 156−159.

(21) Kralchevsky, P. A.; Denkov, N. D. Analytical Expression for the Oscillatory Structural Surface Force. *Chem. Phys. Lett.* **1995**, *240*, 385−392.

(22) Trokhymchuk, A.; Herderson, D.; Nikolov, A.; Wasan, D. T. A Simple Calculation of Structural and Depletion Forces for Fluids/Suspensions Confined in a Film. *Langmuir* **2001**, *17*, 4940−4947.

(23) Basheva, E. S.; Kralchevsky, P. A.; Danov, K. D.; Ananthapadmanabhan, P.; Lips, A. The Colloid Structural Forces as a Tool for Particle Characterization and Control of Dispersion Stability. *Phys. Chem. Chem. Phys.* **2007**, *9*, 5183−5198.

(24) Chengara, A.; Nikolov, A. D.; Wasan, D. T.; Trokhymchuk, A.; Henderson, D. Spreading of Nanofluids Driven by the Structural Disjoining Pressure Gradient. *J. Colloid Interface Sci.* **2004**, *280*, 192−201.

(25) Kondiparty, K.; Nikolov, A.; Wu, S.; Wasan, D. Wetting and Spreading of Nanofluids on Solid Surfaces Driven by the Structural Disjoining Pressure: Statics Analysis and Experiments. *Langmuir* **2011**, *27*, 3324−3335.

(26) Matar, O. K.; Craster, R. V.; Sefiane, K. Dynamic Spreading of Droplets Containing Nanoparticles. *Phys. Rev. E* **2007**, *76* (056315), 1−9.

(27) Oron, A.; Davis, S. H.; Bankoff, S. G. Long-Scale Evolution of Thin Liquid Films. *Rev. Mod. Phys.* **1997**, *69*, 931−980.

(28) Heslot, F.; Fraysse, N.; Cazabat, A. M. Molecular Layering in the Spreading of Wetting Liquid Drops. *Nature* **1989**, *338*, 640−642.

(29) Nikolov, A. D.; Wasan, D. T. Ordered Micelle Structuraling in Thin Films Formed from Anionic Surfactant Solutions. *J. Colloid Interface Sci.* **1989**, *113*, 1−12.

(30) Nikolov, A. D.; Kondiparty, K.; Wasan, D. T. Nanoparticle Self-Structuring in a Nanofluid Film Spreading on a Solid Surface. *Langmuir* **2010**, *26*, 7665−7670.

(31) Nikolov, A. D.; Wasan, D. T. Dispersion Stability Due to Structural Contributions to the Particle Interaction as Probed by Thin Liquid Film Dynamics. *Langmuir* **1992**, *8*, 2985−2994.

(32) Chu, X. L.; Nikolov, A. D.; Wasan, D. T. Effects of Particle Size and Polydispersity on the Depletion and Structural Forces in Colloidal Dispersions. *Langmuir* **1996**, *12*, 5004−5010.

(33) Frenkel, J. *Kinetic Theory of Liquids*; Dover Publications, Inc.: New York, 1955.

(34) Russel, W. B.; Benzing, D. W. The Viscoelastic Properties of Ordered Latices: A Self-Consistent Field Theory. *J. Colloid Interface Sci.* **1981**, *83*, 163−177.

(35) Russel, W. B.; Benzing, D. W. The Viscoelastic Properties of Ordered Latices: Experiments. *J. Colloid Interface Sci.* **1981**, *83*, 178−190.

(36) Besheva, E. S.; Nikolov, A. D.; Krachevsky, P. A.; and Wasan, D. T. Multi-Stepwise Drainage and Viscosity of Macroscopic Films Formed from Latex Suspensions; Mittal, K. L., Shah, D. O., Eds.; *Surfactants in Solution*; Plenum: New York, 1991; Vol. *II*, pp 467−479.